



Comparative Analysis of Seizure Manifestations in Alzheimer's and Glioma Patients via Magnetic Resonance Imaging

Jayanthi Vajiram^{1*}, Sivakumar Shanmugasundaram¹, Rajeswaran Rangasami², Utkarsh Maurya¹

¹ Department of Electronics Engineering, Vellore Institute of Technology Chennai, 600127 Tamil Nadu, India

² Department of Radiology, Sri Ramachandra Medical Centre Chennai, 600116 Tamil Nadu, India

* Correspondence: Jayanthi Vajiram (jayanthi.2020@vitstudent.ac.in)

Received: 09-10-2023

Revised: 10-12-2023

Accepted: 10-20-2023

Citation: J. Vajiram, S. Shanmugasundaram, R. Rangasamim, and U. Maurya, "Comparative analysis of seizure manifestations in Alzheimer's and glioma patients via magnetic resonance imaging," *Inf. Dyn. Appl.*, vol. 2, no. 4, pp. 162–172, 2023. <https://doi.org/10.56578/ida020401>.



© 2023 by the authors. Published by Acadlore Publishing Services Limited, Hong Kong. This article is available for free download and can be reused and cited, provided that the original published version is credited, under the CC BY 4.0 license.

Abstract: A notable association between Alzheimer's Disease and Epilepsy, two divergent neurological conditions, has been established through previous research, illustrating an elevated seizure development risk in individuals diagnosed with Alzheimer's Disease (AD). The hippocampus, fundamental in both seizure and tumour pathology, is intricately investigated herein. The subsequent aberrant electrical activity within this brain region, frequently implicated in seizure onset and propagation, underpins a complex relationship between degenerative cerebral changes and seizure incidence. Symptomatic manifestations in hippocampal glioma include, but are not limited to, seizures, memory deficits, and language difficulties, contingent upon the tumour's location and size. Thus, the cruciality of proficient seizure detection and analysis is underscored. Employing canny edge detection and thresholding to delineate contours and boundaries within images, an analysis was conducted by transmuting grayscale or colour images into a binary format. The input dataset, utilised for the training and testing of machine and deep-learning models, comprised images of seizures. These models were subsequently trained to discern patterns and features within the images, facilitating the differentiation between two predefined classes. Resultantly, the models predicted, with a defined accuracy level, the presence or absence of a seizure within a new image. The Support Vector Machine (SVM) and Convolutional Neural Network (CNN) models demonstrated classification accuracies of 96% and 95%, respectively. By analysing performance metrics on a per-slice basis, the localization of seizure activity within the brain could be visualised, offering valuable insights into regions affected by this activity. The amalgamation of edge detection, feature extraction, and classification models proficiently discriminated between seizure and non-seizure activities, providing pivotal insights for the diagnosis and therapeutic strategies for epilepsy. Further, studying these neurological alterations can illuminate the progression and severity of cognitive and emotional deficits within affected individuals, whilst advancements in diagnostic methodologies, such as Magnetic Resonance Imaging (MRI), facilitate an enriched comparative analysis.

Keywords: Seizure; Canny edge detection; Threshold segmentation; Confusion matrix; AI models

1 Introduction

Gliomas, predominantly found within the central nervous system, emerge in the brain or spine and are invariably linked with tumour formation, provoking symptoms ranging from seizures and headaches to personality alterations. Conversely, Hippocampal Sclerosis (HS), distinguished by a non-standard amount of scar tissue within the hippocampus - an essential region for memory formation - is capable of inducing a spectrum of neurological and cognitive impairments. It has been illuminated through research that HS often coexists with gliomas, especially glioblastoma, which is recognised as the most pervasive and aggressive brain cancer variant and more than 60–70% of dementia cases are under treatment [1]. This nexus is pivotal, suggesting that chronic inflammation or alternative processes within the hippocampus may catalyse the development of certain gliomas. Nonetheless, a more profound exploration and the incorporation of open-source datasets are paramount to scrutinise the precise interrelationship between glioma and HS.

The hippocampus, critical for memory formation, learning, and spatial navigation, is frequently entangled in assorted neurological conditions, encompassing seizures and tumours. Gliomas, accountable for roughly 40% of

all primary brain tumours, can manifest in the hippocampus, besides numerous other cerebral areas, engendering symptoms such as memory issues, headaches, and personality and behavioural transformations. Analyses probing potential treatments and therapies intended to address seizure and tumour pathology, which correlate hippocampal damage with tumour progression, are chronicled within studies [2].

In this investigation, a focus is placed upon the relationship between Alzheimer's disease and glioma, wherein both conditions are capable of inciting Alzheimer's and glioma-related seizures, hence requiring an in-depth examination of the conceivable connection between these two neurological disorders and their unified symptomology of seizures. Comprehensive data collection and a rigorous analysis of the prevalence of seizures in individuals afflicted with Alzheimer's disease and glioma was undertaken. Subsequent methodology for the detection of Seizure affected images from datasets encompassed analysis through canny edge and threshold segmentation process, whilst classification methods included SVMs, logistic regression, AdaBoost, Gradient Boost, Gaussian Naïve base, and CNN models. The methods proposed were evaluated upon a database of seizure-induced MRI images from both datasets. Classifier performance was appraised by gauging the accuracy, sensitivity, specificity, and slice-by-slice analysis, while performance metrics were computed and scrutinised.

Employing canny edge to discern and detect image edges, and thresholding to segregate the hippocampal edges from the background, a combination of the Harris matrix and eigen vector was utilised to detect image features, facilitating a more nuanced and precise segmentation of the hippocampus. It was demonstrated that a) thresholds and canny edges of images can be deployed to identify regions of interest in brain MRI scans for detecting hippocampal anomalies, b) hessian metrics and eigenvalues of images can be employed to segment the hippocampus from the remaining brain, and c) long-term imaging performance analysed by machine learning classifiers and fundamental deep learning architecture can be utilised to monitor glioma progression and assess responses to subsequent treatments. The study underscored that only seizure-affected images were used for early diagnosis. A potential hypothesis for the comparative analysis of seizure induction may postulate: "Distinct patterns of seizure induction, observed on MRI imaging, are attributed to differential neurophysiological changes within the hippocampi of Alzheimer's and glioma patients."

The findings from these methods may augment the diagnostics and treatment of both seizure and tumour pathology, wherein MRI biomarkers emerge as instrumental tools for evaluating hippocampal activity in seizure and tumour pathology, empowering MRI usage for the identification, measurement, and monitoring of alterations in various neurological disorders, including seizures and tumours.

2 Related Study

MRI image datasets, induced by seizures, serve as the analytic foundation for this investigation. The hippocampus, encapsulating regions such as CA1, CA2, CA3, dentate gyrus, and subiculum, is recognized for its multi-faceted functionality, all of which are interlinked through a sophisticated network of neural pathways and neurotransmitters. Moreover, a critical role is played by the hippocampus in modulating the hypothalamic-pituitary-adrenal (HPA) axis, crucial for the formulation and retention of long-term memories. Consequently, impairments to this structure can precipitate deficits in memory, spatial orientation, and navigation. The 2D multi-orientation technique, which includes orientation alignment [3]. A comprehensive understanding of the hippocampus's anatomical features and functionalities becomes imperative for diagnosing and treating neurological and psychiatric disorders.

Pertinent studies have underscored the association between the hippocampus and an array of neurological disorders, inclusive of AD, Parkinson's Disease (PD), tumours, and depression. Furthermore, hippocampal changes have been documented in regular ageing processes and subsequent stress exposure. The delineated patch-based grading (PBG) pattern similarities within hippocampus images, while another study discerned that FPN architecture integrated single-in and single-out, along with multiple-in and multiple-out encoders, employing a divide-and-conquer strategy within their encoder.

The classification of images utilizing CNNs sometimes does not yield accurate outcomes, the ensuing segmentation process might deliver more exact results. To extract object boundaries, edges, and distinguish between all regions of the image, the minimum thickness range of hippocampus sclerosis, lying between 40 and 52 mm, is utilized. Employed for edge identification, threshold canny edge drawing isolates noise without altering original features, identifying edges through a threshold. The resultant edge image presents a difference in the threshold value, determined via supervised learning. Ideal for low-noise images and complex data, edge-based segmentation, in conjunction with the canny edge operator, proves advantageous. Hessian-based multiscale filtering, utilizing convolved 2D or 3D Gaussian filters of eigenvalues, is used to delineate shapes and structures within the images. Gradual loss alterations occur with infinite distance of the eigenvalue of a Hessian matrix, primarily used for image classification and object recognition. This assists in locating a function's local extremum and the saddle points. Hessian matrix 2×2 may possess one or two eigenvalues (positive and negative) and is employed to locate patches in corners with an autocorrelation matrix of eigenvalues. Raw image feature detection is achieved through the second derivative of the Hessian matrix. Both image and scale space local extremum were detected using Hessian

matrices and the difference of Gaussian [4]. Glioma characteristics in the hippocampus in patient MRI scans were compared with T2/FLAIR signal hypointensities and enhanced contrast enhancement. Consideration of the left and right hippocampus is recommended in patients with brain tumours. Glioma and hippocampus cause significant brain functional plasticity, including neural reorganization as determined by transcranial magnetic stimulation [5, 6]. The hippocampus segmentation using machine and deep learning approaches [7].

The relative study clearly shows that the MRI contrast agent is used to detect the abnormalities, and texture of the hippocampus structure. A multi-task deep CNN model can be constructed to simultaneously learn hippocampal segmentation and tumor disease classification. Radiomics classification and prediction can be used for Alzheimer’s Disease and mild cognitive impairment. Furthermore, analyzing hippocampal shape, tumor and asymmetry through cascaded convolutional neural networks can provide valuable insights. Progressive brain tumor atrophy, a key hallmark of AD, can be assessed through temporal and spatial analysis using an improved CNN model and resting-state fMRI data. 3D visualizations of MRI data can meet all of these criteria and enhance accuracy in tumor prediction, as 2D images lack the complete representation in the deep learning analysis [8–16].

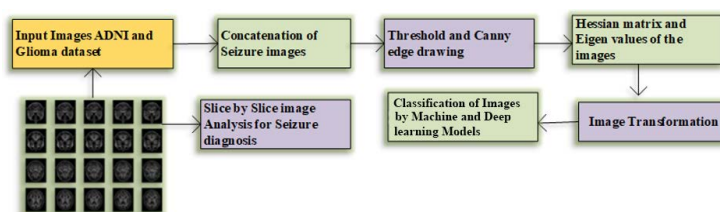


Figure 1. Proposed methodology

In Figure 1, the proposed methodology is elucidated, incorporating the concatenation of seizure images and the application of canny edge detection and threshold segmentation techniques. Subsequently, Hessian matrix eigen vector image transformation is employed to extract pertinent features. A classification algorithm is ultimately deployed to categorize the images, grounded on these extracted features. This strategy facilitates the identification and differentiation of seizure-related patterns within neuroimaging data.

In the context of AD, the emergence of amyloid-beta plaques and neurofibrillary tangles is implicated in the instigation of hippocampus-induced seizures. The analyses articulated in this article draw upon Alzheimer-Hippocampus Sclerosis (AHS) and Lower Grade Glioma (LGG) seizure image datasets. Primary tumours are characterised by cells that originate intrinsically within the hippocampus, whilst secondary tumours proliferate to the hippocampus from disparate brain regions. In instances of AHS, meticulous localization and segmentation of the hippocampus and glioma images can be actualised through the implementation of canny edge and threshold methods. For the detection of tumours and hippocampus regions, canny edge detection is utilised to identify the edges of tumours and hippocampi within an image. Subsequent threshold segmentation is employed to demarcate regions of interest within the image.

3 Methodology

The analysis was conducted on the Alzheimer (AHS) and Glioma (TCIA-LGG) depository datasets. For the detection of seizures within MRI images, the canny edge detection and thresholding methods were employed. The canny edge detection algorithm, in the realm of image processing, identifies pixels with a pronounced gradient magnitude, which correspond to edges. This method is implemented to extract object contours or boundaries for further analysis. Concurrently, thresholding serves as a technique for image binarization by segregating pixels into varying intensity levels, determined by a selected threshold value.

The goal of the study encompasses the classification of whether a presented image contains a seizure. Input datasets, utilized for the training and testing of both machine and deep learning models, presumably comprise images illustrating seizures and images devoid of them. Models are trained to discern patterns and features within these images to distinguish between seizure and non-seizure activities.

The propounded methodology integrates numerous steps for seizure detection, which includes the identification of seizures in MRI images, extraction of pertinent features, classification of MRI images, and a subsequent performance comparison. This methodology holds the potential to proffer invaluable insights for epilepsy diagnosis and treatment, facilitating precise and efficient seizure detection through the analysis of MRI images. A detailed examination of seizure-affected regions in the image is rendered through slice-by-slice image analysis.

For the noise reduction, intensity gradient of the image, non-maximum suppression, double thresholding, and edge tracing by hysteresis, the algorithm is implemented. Thresholding, utilized to differentiate objects in an image based on their intensity values, distinguishes between foreground and background pixels. The canny edge detection method leverages two thresholds: 0.1 and 0.15. The upper limit, 0.15, is implemented to detect edge pixels,

whilst pixels below the lower limit of 0.1 are disregarded. This method facilitates noise reduction, non-maximum suppression, gradient calculation, double thresholding, and hysteresis edge tracking with grayscale images. The noise reduction is enacted through a 5×5 Gaussian filter with a $(2k+1) \times (2k+1)$ kernel size, as expressed in Eq. (1).

$$H_{ij} = \frac{1}{2\pi\sigma^2} \exp\left(-\frac{(i - (k+1))^2 + (j - (k+1))^2}{2\pi\sigma^2}\right); 1 \leq i, j \leq (2k+1) \quad (1)$$

The image gradient can be computed by convolving I with Sobel kernels K_x and K_y , which utilize edge and pixel intensity to identify image edges. Subsequently, the magnitude G and the slope θ of the gradient are determined as presented in Eqs. (3) and (4).

$$K_x = \begin{bmatrix} -1 & 0 & 1 \\ -2 & 0 & 2 \\ -1 & 0 & 1 \end{bmatrix} \quad K_y = \begin{bmatrix} 1 & 2 & 1 \\ 0 & 0 & 0 \\ -1 & -2 & -1 \end{bmatrix} \quad (2)$$

$$\text{Gradient Intensity } |G| = \sqrt{I_x^2 + I_y^2} \quad (3)$$

$$\text{Edge direction } \theta(x, y) = \arctan \frac{I_x}{I_y} \quad (4)$$

3.1 Hessian Metric and Eigenvalues in Image Analysis

The Hessian matrix, a symmetric matrix, is elucidated as representing the actual eigenvalues of a 2D image's orthogonal coordinate system, with the nuances of second-order image intensity variations being circumscribed around the voxel point. To facilitate its computation, initial image smoothing is necessitated to mitigate noise, followed by the employment of numerical approximations of the second-order partial derivatives I_{xx} , I_{yy} , and I_{xy} . This approach assists in revealing the direction of the gradient curve of the image.

The Gaussian function $G(x, y)$ is implemented as a smoothing function:

$$G(x, y, \sigma) = \frac{1}{2\pi\sigma^2} e^{-\frac{(x^2+y^2)}{2\sigma^2}} \quad (5)$$

The partial derivative in x of Eq. (5), denoted as G_x , is computed as:

$$\frac{\partial G(x, y, \sigma)}{\partial x} = -\frac{x}{2\pi\sigma^4} e^{-\frac{(x^2+y^2)}{2\sigma^2}}$$

Consequently, I_x can be attained by filtering the image with the aforementioned function. Employing $x, y = [-3\Sigma : 3\Sigma]$ as the filtering mask, the partial derivative is obtained through image convolution with the mask.

The convolution masks for I_{xx} , I_{yy} and I_{xy} , given by Eqs. (6)-(8) respectively, can be expressed as follows.

$$\frac{\partial^2 G(x, y, \sigma)}{\partial^2 x} = \left(-1 + \frac{x^2}{\sigma^2}\right) \frac{e^{-\frac{(x^2+y^2)}{2\sigma^2}}}{2\pi\sigma^4} \quad (6)$$

$$\frac{\partial^2 G(x, y, \sigma)}{\partial^2 y} = \left(-1 + \frac{y^2}{\sigma^2}\right) \frac{e^{-\frac{(x^2+y^2)}{2\sigma^2}}}{2\pi\sigma^4} \quad (7)$$

$$\frac{\partial^2 G(x, y, \sigma)}{\partial xy} = \left(\frac{xy}{2\pi\sigma^6}\right) e^{-\frac{(x^2+y^2)}{2\sigma^2}} \quad (8)$$

In a multi-scale approach, this formulation proves beneficial to acquire the Hessian matrix at disparate scales, as illustrated in Figure 2.

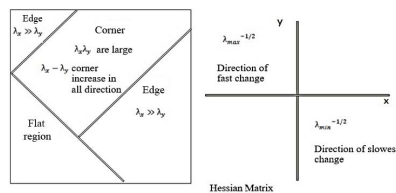


Figure 2. Representation of the hessian metric and eigenvalues

The Hessian metric, a measurement of a function’s curvature, is defined by the second partial derivatives of the function with respect to its independent variables. The eigenvalues of the Hessian matrix are intrinsically tied to the curvature of the function; negative eigenvalues indicate concavity, while positive ones denote convexity. In Figure 2, the Hessian metric is exemplified as a matrix with two eigenvalues, both of which are negative, indicating a concave function. The eigenvalues can be harnessed to ascertain the stability of the function: dual negative eigenvalues suggest stability, while the presence of a positive eigenvalue implies instability. The focal loss function was employed for the classification of the CNN model.

The implementation of Balanced Cross Entropy (BCE) is defined as follows:

$$BCE = \sum_i (Y_i \ln(P_i) + (1 - Y_i) \ln(1 - P)) \quad (9)$$

with the understanding that $(1 - P_i)^\gamma$ represents the cross-entropy loss, featuring a tunable focusing parameter $\gamma \geq 0$. A specific instance of the focal loss, P_i , is articulated as:

$$P_i = (\alpha_i (1 - P_i)^\gamma \log P_i) \quad (10)$$

Crucially, P_i remains unaffected in scenarios of minor loss and approaches zero in situations where wellclassified examples are down-weighted in the model.

Eigenvalues of the Hessian matrix find utility in altering the gradient of a loss function, enabling an infinitesimal progression in a prescribed direction. This adjustment of the gradient, achieved through the usage of Hessian matrix eigenvalues, enhances model stability by amplifying the penalty applied to high-loss, negative samples. Therefore, the model can navigate an infinite distance in a designated direction, thus fortifying its stability and honing its focus on complex examples, as depicted in Figure 3, which illustrates the impact of epilepsy induced by glioma and Alzheimer-affected MRI images.

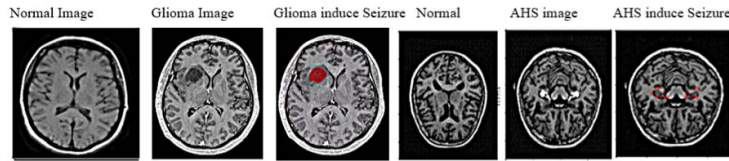


Figure 3. Illustration of epilepsy induced by glioma and Alzheimer affected MRI images

The segmented hippocampus, discernible on both left and right aspects, is exhibited in Figure 4 subsequent processes involve the utilization of a canny edge detector for the identification and tracking of image edges, followed by threshold segmentation to ascertain regions of interest within the image. The culmination of this methodology is the concatenation of the hippocampus, entailing the fusion of its bifurcated sides, thereby facilitating a more accurate representation for ensuing analysis. The image dimensions of (233, 197, 3) signify a width of 233 pixels, a height of 197 pixels, and the incorporation of 3 colour channels (RGB).

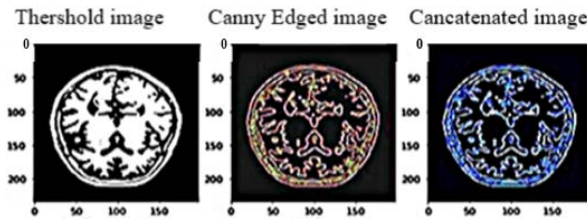


Figure 4. Canny edge and threshold segmentation

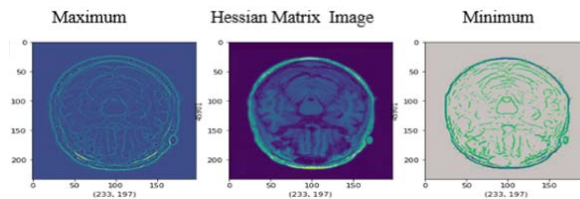


Figure 5. Hessian matrix of AHS images

In Figure 5, the Hessian metric and eigenvalues of maximum and minimum images are presented. The Hessian matrix, a 3×3 matrix, is employed to compute the local curvature of a surface. Eigenvalues serve as indicators, signifying whether the surface under examination is convex (two positive eigenvalues and one negative) or concave.

Contrastingly, Figure 6 reveals the results of applying canny edge and threshold segmentation to normal and glioma images. The methodology empowers the detection and identification of alterations in the brightness or colour between normal and glioma tissue. Normal imagery reveals a more uniform gradient of brightness, whereas glioma imagery exposes more conspicuous edges. Prominent white edges indicate regions where brightness or colour deviates significantly, offering a technique that efficiently identifies tissue alterations.

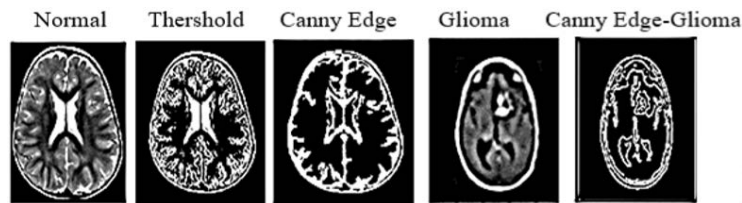


Figure 6. Canny edge and threshold segmentation

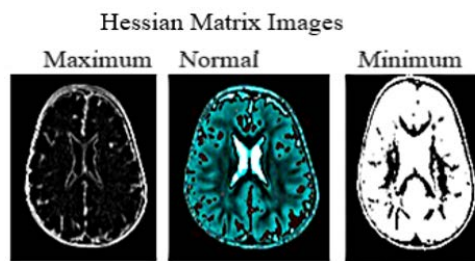


Figure 7. Hessian matrix of glioma images

Lastly, Figure 7 demonstrates that the Hessian metric assists in more accurately identifying tumour regions due to its proficient detection of tumour boundaries when compared to alternative methods. Additionally, eigenvalues of the Hessian matrix can serve to measure the texture of tumour regions, facilitating the differentiation between varied tumour types.

3.2 Elbow Method for Optimal Cluster Determination

The application of the Elbow method, instrumental in discerning the optimal number of clusters pertinent to a particular dataset, hinges on the principle that the total within-cluster sum of squares (WCSS) progressively diminishes as the number of clusters augments. Esteemed studies have demonstrated the efficacy of the Elbow method in ascertaining the optimal number of clusters in diverse data types, such as gene expression data, MRI data, and genomic data. Insights derived from the outcomes of the Elbow method have catalyzed the establishment of a classification system for LGGs and AHS, alongside the identification of biomarkers integral to disparate subtypes of images.

In Figure 8, a graphic representation delineating the Elbow method — a juxtaposition of the number of clusters against the cost function — is illustrated. The horizontal and vertical axes epitomize the number of clusters and the value of the cost function (cs), respectively. This cost function is methodically determined by gauging the sum of squared errors (SSE) within each cluster, with SSE being computed by tallying the squared distances between each constituent point within a cluster and the cluster centre. The optimal cluster number emerges at the graph's inflection point, where the cost function's reduction rate commences to plateau, coined as the “elbow” of the graph. This pivotal point implies that the incorporation of supplementary clusters will not substantially mitigate the cost function.

The Elbow method, as delineated by Kodinariya, is strategically deployed to discern the optimal number of clusters within a dataset, executed by graphing the SSE across varying values of the cluster number k . A decreasing trend is observed in SSE as k is incremented; however, beyond a certain point, the decrement in SSE is not sufficiently substantial to warrant the incorporation of additional clusters. The juncture at which this decrement in SSE ceases to be noteworthy is heralded as the optimal cluster number. Consequently, a discernible inflection at $k=2$ in the aforementioned plot suggests potential optimality in employing two clusters for data classification in the context presented.

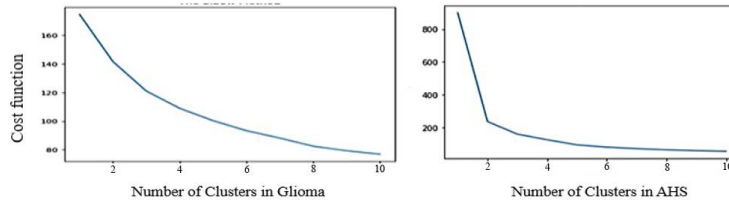


Figure 8. Elbow method graph illustrating clusters versus cost function

Notably, the K-means clustering algorithm, which organizes data points into clusters predicated on their analogous characteristics, can be judiciously exploited to segment images by congregating similar pixels. Subsequently, this clustering outcome can facilitate the identification of variant tissue types within an image, thus serving as a potent tool in biomedical image analysis and classification.

4 Results and Analysis of Epilepsy Images

In the realm of epileptic imaging analysis, machine learning and elementary deep learning classifiers have been employed to scrutinize model outputs. SVMs, representing a class of supervised learning models, are fabricated to instantiate a hyperplane or an ensemble of hyperplanes within a high- or infinitely-dimensional space. Concurrently, logistic regression is utilised to delineate the decision boundary, which subsequently bifurcates the data into binary classes.

An ensemble learning algorithm, AdaBoost amalgamates multiple weak learners into a singular, robust learner. Herein, the weak learners typically manifest as decision trees, characterised by a single bifurcation, referred to as decision stumps. The model sequentially accentuates the observations, prioritising the instances that are challenging to classify while mitigating focus on those effectively handled. As this iterative process unfolds, sample weights are modified individually, culminating in the formation of a final model after numerous iterations. Conversely, the Gradient Boost model is synthesised through the amalgamation of several weaker models, wherein each contributes to the model’s predictive prowess.

The Gaussian Naive Bayes, deploying a Gaussian distribution, estimates the probability of each class given the data features and in turn, demarcates the decision boundary, thereby segregating the data into two distinct classes.

A quintessential CNN architecture is formulated of assorted layers, each executing a distinctive function, orchestrated to synergistically construct a representation of the input data. Comprising convolutional layers, pooling layers, fully connected layers, and normalization layers, these intricately structured networks utilise the output from each layer to facilitate predictions or classifications pertaining to the input data. The efficacy of region-based active contours and graph-cuts in calculating accuracies has also been explored. CNNs have been the optimal choice for the automated detection of hippocampus segmentation. The IDH1 wild-type glioblastoma used to assess hippocampus resilience in brain tumor [17, 18]. Furthermore, an amalgamation of a 3D CNN and a 2D CNN has been investigated to enhance accuracy.

MATLAB has been prevalently utilised for the execution of regression and classification metric predictions on individual images. While CNNs have demonstrated significant efficacy in tasks necessitating substantial data and pattern identification within images, traditional machine learning classifiers have emerged as more appropriate for simpler tasks that demand less data and hinge predominantly on data features.

4.1 Evaluation Metrics Employed in Analysing Seizure Imagery

Utilisation of logistic regression metrics for the computational assessment of the probability affiliated with a given 2D image being categorised into a specific class or outcome emerges as pivotal, especially when discerning the likelihood of particular conditions or diseases based on distinct sets of characteristics. In this context, Table 1 delineates the regression scores, distinguishing between normal and seizure-impacted images, while Figure 9 demonstrates the performance matrix.

Performance metrics, including accuracy, precision, recall, and f-measure, for individual 2D images have been computed. These metrics serve as valuable tools for evaluating diagnostic accuracy, offering insights into potential areas necessitating enhancement. Thus, the efficacy of specific methodologies in detecting and categorising distinct seizure activities at the image level is ascertained.

Details pertaining to classification performance matrices are revealed in Table 2, Figure 9, and Figure 10. It is suggested that an increase in the number of slices correlates to an enhancement in analysis detail and a reduction in the number of seizure pixels. Consequently, Figure 11 shows cases the relationship between slice quantity and the average count of seizure pixels, contributing to the diagnostics and treatment approaches for epilepsy.

Table 1. Regression metrics for normal, masked, and seizure images

Images	SNR	Peak-SNR	MSE	SSIM	Salt and Pepper Noise Method		
					SNR	Peak-SNR	MSE
Normal Image	14.8877	19.1768	106.6993	0.8688	35.6855	40.0119	277.5116
Masked Image	14.5632	19.0679	105.3979	0.8661	42.2295	46.7714	284.4962
Seizure Image	13.3925	18.7648	103.5315	0.8577	36.1346	41.5338	298.8684

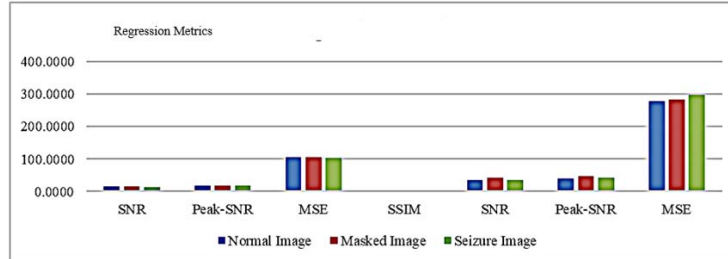


Figure 9. Regression model-driven performance metrics of seizure imagery

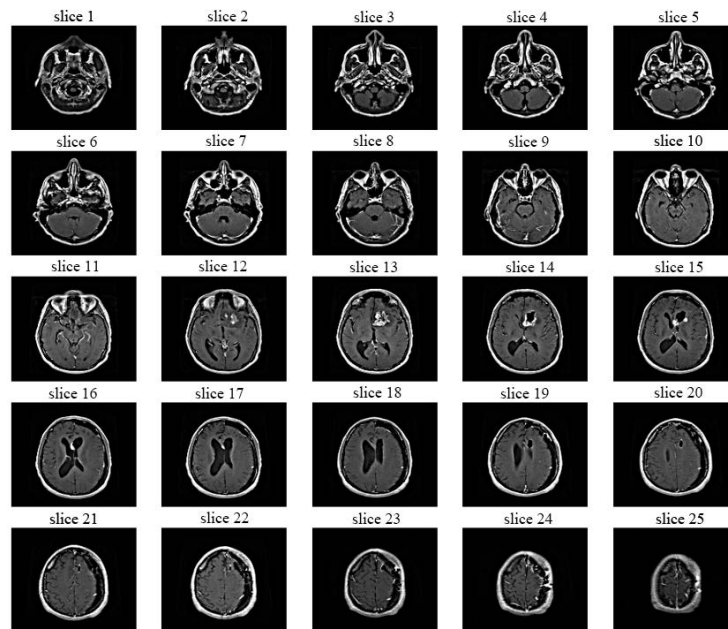


Figure 10. Analysis of epilepsy-affected imagery by slice number

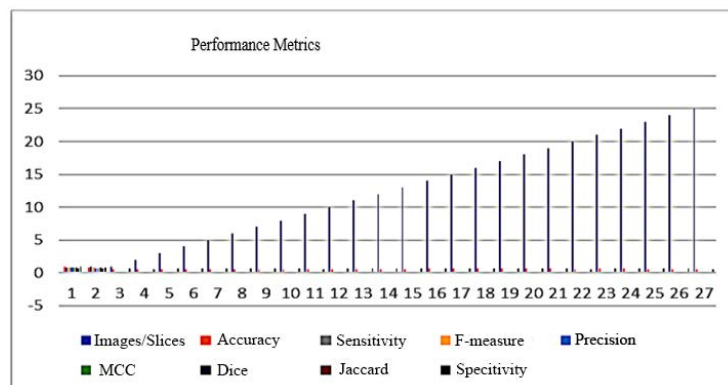


Figure 11. Performance metrics for seizure imagery

Table 2. Slice-by-Slice calculation of performance metrics

Images	Accuracy	Sensitivity	F-measure	Precision	MCC	Dice	Jaccard	Specificity
Normal Image	0.8977	0.8701	0.8569	0.8356	0.8569	0.8569	0.7456	0.9075
Seizure Image	0.8765	0.9359	0.8087	0.7120	0.7347	0.8087	0.6789	0.8536
Slice1	0.6063	0.0748	0.0120	0.0065	-0.1099	0.0120	0.0060	0.6238
Slice2	0.6022	0.0669	0.0120	0.0066	-0.1202	0.0120	0.0060	0.6222
Slice3	0.6106	0.0632	0.0084	0.0045	-0.1032	0.0084	0.0042	0.6253
Slice4	0.6100	0.0690	0.0095	0.0051	-0.1033	0.0095	0.0048	0.6251
Slice5	0.6103	0.0750	0.0103	0.0056	-0.1011	0.0103	0.0052	0.6253
Slice6	0.6143	0.0959	0.0116	0.0062	-0.0875	0.0116	0.0058	0.6268
Slice7	0.6100	0.0690	0.0084	0.0051	-0.1202	0.0084	0.0116	0.6268
Slice8	0.6176	0.0646	0.0061	0.0032	-0.0852	0.0061	0.0031	0.6278
Slice9	0.6082	0.0669	0.0120	0.0066	-0.1202	0.0120	0.0060	0.6222
Slice10	0.6195	0.0368	0.0029	0.0015	-0.0844	0.0029	0.0014	0.6284
Slice11	0.6194	0.0578	0.0578	0.0025	-0.0812	0.0048	0.0024	0.6284
Slice12	0.6220	0.0875	0.0064	0.0033	-0.0686	0.0064	0.0032	0.6295
Slice13	0.6225	0.0500	0.0032	0.0016	-0.0727	0.0032	0.0016	0.6295
Slice14	0.6231	0.0187	0.0011	0.00054638	-0.0752	0.0011	5.31E-04	0.6296
Slice15	0.6232	0.023	1.30E-03	6.70E-04	-0.0741	1.30E-03	6.52E-04	0.6297
Slice16	0.6229	0.0285	1.70E-03	8.66E-04	-0.0745	1.70E-03	8.41E-04	0.6296
Slice17	0.6291	0.0485	0.0012	6.29E-04	-0.0457	0.0012	6.21E-04	0.6319
Slice18	0.6321	0.0529	4.11E-04	2.06E-04	-0.0246	4.11E-04	2.05E-04	0.633
Slice19	0.6322	0.0182	1.23E-04	6.19E-05	-0.0255	1.23E-04	6.16E-05	0.633
Slice20	0.6022	0.0669	1.20E-02	6.60E-03	-0.1202	1.20E-02	6.00E-03	0.6222
Slice21	0.6324	0.0038	2.06E-05	1.03E-05	-0.0236	2.06E-05	1.03E-05	0.633
Slice22	6.23E-01	8.70E-02	0.0057	3.00E-03	-6.53E-02	0.0057	0.0029	0.6299
Slice23	0.616	0.1687	0.0226	0.0121	-0.0675	0.0226	0.0114	0.6281
Slice24	0.6057	9.67E-02	1.66E-02	0.0091	-0.1057	0.0166	0.0084	0.6238
Slice25	0.5963	5.20E-03	9.73E-04	5.36E-04	-0.1481	9.73E-04	4.87E-04	0.6193

Table 3. Performance metrics calculated utilising various classifier models

Machine Learning Models	Accuracy (%)	Sensitivity	Specificity
SVM	96.83	0.952	0.9319
Logistic Regression	91.67	0.801	0.6311
AdaBoost	94.36	0.499	0.7541
Gaussian Naïve Bayes	93.54	0.971	0.6333
Gradient Boosting	94.20	0.972	0.5454
Deep Learning Models	Accuracy (%)	Sensitivity	Specificity
CNN Architecture	95.98	0.905	0.848
DNN Architecture	94.03	0.654	0.752

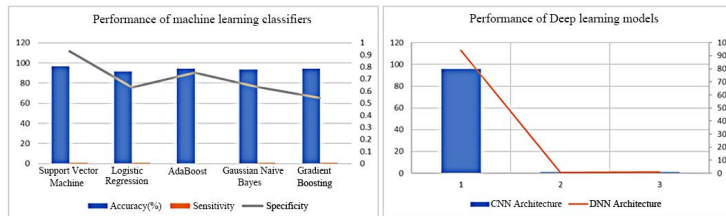


Figure 12. Classifier model-driven performance of seizure imagery

The prediction of seizure images, as elucidated by the confusion matrix in Table 3, Figure 12, and Figure 13, encapsulates the enumeration of true positives, true negatives, false positives, and false negatives, for both validation and test sets. A pivotal revelation from the research establishes a significant association between hippocampal

alterations and emotional deficits, inclusive of memory impairments, learning difficulties, mood disorders, and emotional instability. This discovery accentuates the imperative nature of probing and comprehending the role of the hippocampus in tumour disorders, potentially guiding the evolution of targeted interventions and treatment strategies.

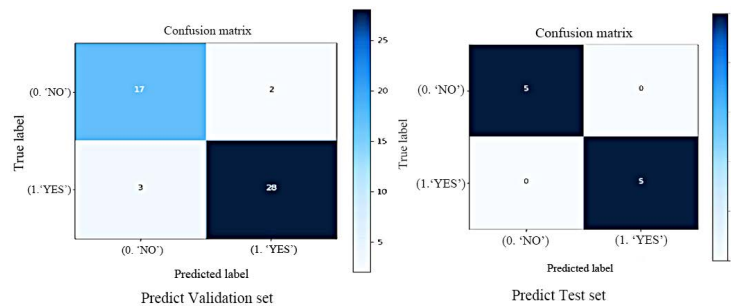


Figure 13. Predictions using validation and test sets with deep learning models

5 Conclusions

An examination has been conducted into the relative impacts of seizures, with a focal point on those induced by hippocampal alterations, a region demonstrated to be more susceptible to seizures in contrast to the glioma. Discrepancies in both magnitude and character of seizures between the two aforementioned conditions have been meticulously explored. Insight has been gleaned into the varying susceptibility of the hippocampus and glioma to seizures, furnishing an avenue to enhance understanding regarding the mechanisms underpinning seizure origination within these contexts. It is posited that the deployment of precise pharmacological interventions to govern seizure activity may serve to mitigate the likelihood of subsequent cognitive deterioration. Extensive and impactful future research vistas are envisioned, centred on the analysis of clinical datasets to discern alterations within the hippocampus.

Author Contributions

Jayanthi Vajiram is responsible for conceptualization, methodology, writing—original draft preparation, Sivakumar Shanmugasundaram is responsible for formal analysis, Rajeswaran Rangasami is responsible for data curation and checking, and Utkarsh Maurya is supported for software validation. All authors have read and agreed to the published version of the manuscript. The relevant terms are explained at the CRediT taxonomy.

Data Availability

(a) ADNI dataset contains MRI (3mm, T1w) with coronal, sagittal, and axial plain images used for segmentation of the Hippocampus gland with two parts. The first part 100 patient images used as train data and the second part contains images of 35 patients as test data [19]. (b) LGG dataset [20] has brain MRI images together with manual FLAIR abnormality segmentation masks of low-grade glioma-affected patients (110) in the Cancer Genome Atlas [TCIA-LGG]. (c) The dataset of seizure-affected images is collected from as DICOM images (500 Seizure affected +2000 normal images) a total of 2500 images are used for this study.

Conflicts of Interest

The authors declare that they have no conflicts of interest.

References

- [1] L. Huang, S. Chao, and C. Hu, "Clinical trials of new drugs for Alzheimer disease," *J. Biomed. Sci.*, vol. 27, no. 1, pp. 1–13, 2020. <https://doi.org/10.1186/s12929-019-0609-7>
- [2] E. Yim, "Tumor burden-dependent hippocampal-dependent memory impairment in a mouse model of glioma," *Sci. Rep.*, vol. 9, no. 1, 2019. <https://doi.org/10.1038/s41598-019-46552-4>
- [3] D. Carmo, B. Silva, C. Yasuda, L. Rittner, and R. Lotufo, "Hippocampus segmentation on epilepsy and Alzheimer's disease studies with multiple convolutional neural networks," *Heliyon*, vol. 7, no. 2, 2021. <https://doi.org/10.1016/j.heliyon.2021.e06226>
- [4] B. Lin, Y. Sun, J. E. Sanchez, and X. Qian, "Efficient vessel feature detection for endoscopic image analysis," *IEEE Trans. Biomed. Eng.*, vol. 62, no. 4, pp. 1141–1150, 2014. <https://doi.org/10.1109/TBME.2014.2373273>
- [5] C. Le Fevre, X. Cheng, M. P. Loit, A. Keller, H. Cebula, D. Antoni, A. Thiery, J. M. Constans, F. Proust, and G. Noel, "Role of hippocampal location and radiation dose in glioblastoma patients with hippocampal atrophy," *Radiat. Oncol.*, vol. 16, no. 112, 2021. <https://doi.org/10.1186/s13014-021-01835-0>

- [6] K. Lv, X. Cao, R. Wang, P. Du, J. Fu, D. Geng, and J. Zhang, "Neuroplasticity of glioma patients: Brain structure and topological network - review," *Front. Neurol.*, vol. 13, 2022. <https://doi.org/10.3389/fneur.2022.871613>
- [7] P. Yi, L. Jin, T. Xu, L. Wei, and G. Rui, "Hippocampal segmentation in brain MRI images using machine learning methods: A survey," *Chin. J. Electron.*, vol. 30, no. 5, pp. 793–814, 2021. <https://doi.org/10.1049/cje.2021.06.002>
- [8] J. Wahsner, E. Gale, A. Rodríguez-Rodríguez, and P. Caravan, "Chemistry of MRI contrast agents: Current challenges and new frontiers," *Chem. Rev.*, vol. 119, no. 2, pp. 957–1057, 2018. <https://doi.org/10.1021/acs.chemrev.8b00363>
- [9] X. Feng, J. Yang, A. F. Laine, and E. D. Angelini, "Alzheimer's disease diagnosis based on anatomically stratified texture analysis of the hippocampus in structural MRI," in *IEEE 15th International Symposium on Biomedical Imaging*. Washington DC, USA, 2018, pp. 1546–1549. <https://doi.org/10.1109/ISBI.2018.8363868>
- [10] M. Liu, F. Li, H. Yan, K. Wang, Y. Ma, L. Shen, and M. Xu, "A multi-model deep convolutional neural network for automatic hippocampus segmentation and classification in Alzheimer's disease," *NeuroImage*, vol. 208, p. 116459, 2020. <https://doi.org/10.1016/j.neuroimage.2019.116459>
- [11] Q. Feng and Z. Ding, "MRI radiomics classification and prediction in Alzheimer's disease and mild cognitive impairment: A review," *Curr. Alzheimer Res.*, vol. 17, no. 3, pp. 297–309, 2020. <https://doi.org/10.2174/1567205017666200303105016>
- [12] A. Li, F. Li, F. Elahifasae, M. Liu, and L. Zhang, "Hippocampal shape and asymmetry analysis by cascaded convolutional neural networks for Alzheimer's disease diagnosis," *Brain Imaging Behav.*, vol. 15, no. 5, pp. 2330–2339, 2021. <https://doi.org/10.1007/s11682-020-00427-y>
- [13] K. Kwak, W. Stanford, and E. Dayan, "Identifying the regional substrates predictive of Alzheimer's disease progression through a convolutional neural network model and occlusion," *Hum. Brain Mapp.*, vol. 43, no. 18, pp. 5509–5519, 2022. <https://doi.org/10.1002/hbm.26026>
- [14] H. Sun, A. Wang, and S. He, "Temporal and spatial analysis of Alzheimer's disease based on an improved convolutional neural network and a resting-state fMRI brain functional network," *Int. J. Environ. Res. Public Health*, vol. 19, no. 8, p. 4508, 2022. <https://doi.org/10.3390/ijerph19084508>
- [15] C. R. Madan, "Creating 3D visualizations of MRI data: A brief guide," *F1000Res*, vol. 4, p. 466, 2015. <https://doi.org/10.12688/f1000research.6838.1>
- [16] N. Hamzah, N. Alias, S. A. Wahab, and Z. A. Omar, "3D model visualization for brain tumour using MRI images," *Journal of Physics: Conference Series*, vol. 1358, p. 012062, 2019. <https://doi.org/10.1088/1742-6596/1358/1/012062>
- [17] A. Zilioli, F. Misirocchi, C. Mutti, B. Pancaldi, E. Mannini, M. Spallazzi, L. Parrino, D. Cerasti, M. Michiara, and I. Florindo, "Volumetric hippocampal changes in glioblastoma: A biomarker for neuroplasticity," *J. Neurooncol.*, vol. 163, pp. 261–267, 2023. <https://doi.org/10.1007/s11060-023-04315-5>
- [18] J. V. Manjón, J. E. Romero, and P. Coupe, "A novel deep learning based hippocampus subfield segmentation method," *Sci. Rep.*, vol. 12, p. 1333, 2022. <https://doi.org/10.1038/s41598-022-05287-8>
- [19] "Alzheimers-disease-5-class-dataset-adni," 2021. <https://www.kaggle.com/datasets/madhucharan/alzheimers-disease5classdatasetadni/data>
- [20] M. A. Mazurowski, K. Clark, N. M. Czarnek, P. Shamsesfandabadi, K. B. Peters, and A. Saha, "Radiogenomics of lower-grade glioma: Algorithmically-assessed tumor shape is associated with tumor genomic subtypes and patient outcomes in a multi-institutional study with The Cancer Genome Atlas data," *J. Neurooncol.*, vol. 133, pp. 27–35, 2017. <https://doi.org/10.1007/s11060-017-2420-1>